Applied Catalysis B: Environmental 190 (2016) 125–136

Contents lists available at ScienceDirect

Applied Catalysis B: Environmental

journal homepage: www.elsevier.com/locate/apcatb

Synthesis, characterisation and behaviour of Co/hydroxyapatite catalysts in the oxidation of 1,2-dichloroethane

Zouhair Boukha*, Jonatan González-Prior, Beatriz de Rivas, Juan R. González-Velasco, Rubén López-Fonseca, José I. Gutiérrez-Ortiz

Chemical Technologies for Environmental Sustainability Group, Department of Chemical Engineering, Faculty of Science and Technology, University of The Basque Country UPV/EHU, P.O. Box 644, E-48080 Bilbao, Spain

ARTICLE INFO

Article history:
Received 24 November 2015
Received in revised form 28 February 2016
Accepted 4 March 2016
Available online 8 March 2016

Keywords:
Hydroxyapatite
Ion-exchanged Co^{2+}
Co_3O_4
Surface chemistry
DCE total oxidation

ABSTRACT

Calcium-deficient hydroxyapatite (HAP) loaded with different amounts of cobalt are synthesised and characterised by several techniques including N_2 physisorption, XRD, TEM, H_2-TPR, UV–vis-NIR DRS, XPS spectroscopy and volumetric adsorption of CO_2 and NH_3 molecules techniques. The Co(x)/HAP catalysts are tested in the oxidation of 1,2-dichloroethane. Due to significant enhancement of the textural and structural properties the resulting Co/hydroxyapatite catalysts achieve higher activity compared to bulk Co_3O_4 catalyst confirming the advantage of dispersing cobalt on a relatively high surface area HAP. Hydroxyapatite support shows a high selectivity towards intermediate reaction products; but its activity suffers a significant decay with time due to chlorination. However, high stability and high selectivity towards deep oxidation products are favoured by Co-rich catalysts.

1. Introduction

Due to the increasing awareness of the negative effects of emissions of volatile organic compounds (VOCs) the industrialised countries governments are imposing rigorous legislations. The essential objective is to minimise these emissions under specific standards in order to maintain the equilibrium in the global energy balance and to reduce direct health risks [1–3]. The presence of chlorine atoms in the chemical structure makes them even more resistant to degradation [2–4]. These chlorinated VOCs (Cl-VOCs) are essentially associated with different industrial activities which release a wide variety of molecular compounds. The Cl-VOCs generally include polychloromethanes, polychloroethanes and polychloroethylenes compounds which possess high volatility and strong resistance to destruction [2–5].

Though a number of studies dealing with remediation technologies for removal and decomposition of Cl-VOCs are presently available [6–10], thermal incineration is considered by far the most effective strategies [2,7]. However, it requires high operation temperatures (>700 °C), thereby increasing the processing cost and NO_x emissions. To overcome these drawbacks the catalytic oxidation appears to be a good alternative allowing lower operating temperatures and better control of the reaction products [11–18]. Thus, the synthesis of active and stable catalysts for Cl-VOCs oxidation at low temperature and with high selectivity towards complete oxidation products, i.e. CO_2, H_2O and HCl/Cl_2 is receiving increasing attention in the literature [11–18].

A considerable number of suitable catalytic systems, including noble metals [19–21] and transition metals [11,12,14,22–24], have been investigated for total oxidation of chlorinated compounds. As major drawbacks of expensive noble metals are adsorption of chlorine species on the active surface and sintering of the metal active sites at high temperatures [14]. Transition metal oxides (V, Cr, Mn, Fe, Co, Ni, Cu, Zn, Nb, and Mo) appear as a good alternative to noble metal catalysts because of their low cost and their resistance to chlorine poisoning [2,11,12,14,24].

Despite their high activity in the oxidation of hydrocarbons and carbon monoxide cobalt catalysts have scarcely attracted attention concerning their applicability in the removal of chlorinated volatile compounds. The few available investigations dealing with this formulation demonstrated their promising performance for Cl-VOCs removal [11,12,14]. We previously studied the catalytic performance of a series of bulk Co_3O_4 catalysts prepared by a variety of routes in the gas-phase oxidation of 1,2-dichloroethane [11], resulting in considerably higher activity and stability than supported noble metals (Pt, Pd), protonic zeolites, and Ce/Zr and Mn/Zr mixed oxides. This catalytic performance of bulk Co_3O_4 catalysts

* Corresponding author.
E-mail addresses: zouhair.boukha@ehu.eus, zouhair.boukha@hotmail.com (Z. Boukha).

http://dx.doi.org/10.1016/j.apcatb.2016.03.005
0926-3373/

was related to the oxygen mobility and the acid character of surface active sites. In this sense, Cai et al. [14] studied the influence of modifying the Co_3O_4 structure, by incorporation of small amount of Mn, on the catalytic activity in the oxidation of 1,2-dichlorobenzene. They reported that Mn species retarded the oxygen mobility of surface active oxygen and increased Co^{2+} concentration which had a positive effect on activity, selectivity and stability of $Mn_xCo_{3-x}O_4$ catalyst.

Though less detailed and numerous, some papers dedicated to this environmental application have also dealt with the textural properties improvement of Co_3O_4 by means of its dispersion on conventional supports (alumina, zeolite, SiO_2). However, it was proved that this route significantly reduces the activity due to the formation of inactive Co species. For example, Chintawar et al. [25] reported that Co loaded zeolite Y and alumina catalysts were not feasible for the complete catalytic oxidation of chlorinated ethylenes. Generally, in the case of cobalt alumina supported catalysts, an interaction between cobalt oxide and catalyst support could result in incorporation of some Al^{3+} ions into Co_3O_4 spinel matrix resulting in $Co^{2+}Co^{3+}{}_{2-x}Al_xO_4$ mixed spinels which would hinder the reduction of Co_3O_4 particles and their oxygen mobility capacity [25,26].

Hydroxyapatite, $Ca_{10}(PO_4)_6(OH)_2$ (HAP), has been intensively investigated as porous support [27–34]. The interest was justified by the presence of phosphate groups which stabilise the structure of active sites and allow the tuning of acid-base properties by varying the calcium/phosphorus ratio. Moreover, the ability of hydroxyapatite to undergo cation and anion exchanges, due to the presence of two types of zeolite-like channels, leads to modulate its chemical properties without damaging its typical hexagonal structure [28]. These characteristics confer to hydroxyapatite catalysts the generation of new synergic metal-support interactions which could improve their catalytic activity [35–41]. Particularly Moffat's group [35,40] found promising results on the destruction of chlorinated compounds over this type of catalysts.

The aim of this work is the investigation of the textural, structural, surface chemistry and catalytic behaviour of a series of calcium deficient hydroxyapatite-supported cobalt samples in the total oxidation of 1,2-dichloroethane (DCE), selected as one of the most important chlorinated pollutants emitted in gaseous industrial waste streams [3,11]. The choice of HAP was made because of the possibility of the control of the Co-support interaction. In this sense, due to its low capacity to exchange Co^{2+} ions (< 1.4%) it was expected that this might limit the aforementioned loss of Co active phase compared to conventional supports. The characterisation of the prepared samples involved a wide number of techniques including BET, TEM, XRD, H_2-TPR, FTIR, UV–vis-NIR DRS, XPS spectroscopy and volumetric adsorption of NH_3 and CO_2 as well-known probe molecules for acid and basic sites, respectively. Cobalt ion-exchanged hydroxyapatite catalyst is also prepared in order to be used as reference. To the best of our knowledge, the applicability of these catalytic materials in the gas-phase oxidation of DCE reaction has not been yet investigated.

2. Experimental

2.1. Preparation of the catalysts

Hydroxyapatite support (HAP) was synthesised adding dropwise a boiling aqueous solution of calcium nitrate to a solution of $(NH_4)_2HPO_4$. The precipitate was re-dissolved in a nitric acid solution and neutralised with ammonia at pH 10. The resulting mixture was maintained under stirring at 80 °C for 16 h. After filtration, the recovered solid was thoroughly washed with purified water, then dried at 120 °C and finally calcined at 500 °C for 4 h.

Cobalt loaded HAP catalysts were prepared by incipient wetness impregnation using solutions containing varying amounts of $Co(NO_3)_2{\cdot}6H_2O$. The impregnated samples were dried in air at 110 °C for 12 h and subsequently calcined for 4 h, at 500 °C. The resulting samples will be hereafter referred as Co(x)/HAP. The loaded amount of cobalt was represented by 'x' and it corresponded to the actual Co weight percentage in the catalyst. The final chemical composition was confirmed by means of ICP analysis.

An ion-exchanged sample, Co(IE)-HAP, was also prepared at room temperature by introducing 10 g of HAP into 1000 cm^3 of aqueous solution containing $Co(NO_3)_2{\cdot}6H_2O$ (2 g). After stirring for 24 h the solid recovered after filtration was washed, dried at 120 °C and finally calcined at 500 °C.

2.2. Characterisation techniques

The volumetric N_2 adsorption at −196 °C was performed on an automatic apparatus Micromeritics, model TRISTAR II 3020 apparatus. The pre-treatments applied to the samples consisted of a cleaning, at 300 °C (overnight), under nitrogen flow. The specific areas of the samples were determined in line with the standard BET procedure, using nitrogen adsorption taken in the relative equilibrium pressure interval of 0.03–0.3.

X-ray diffraction (XRD) studies were conducted on a X'PERT-MPD X-ray diffractometer with Cu Kα radiation (λ = 1.5406 Å) and Ni filter. The X-ray tube was operated at 40 kV and 40 mA. The samples were scanned between 10° and 100° (2θ), and the X-ray diffraction line positions were determined with a step size of 0.01° and a counting time of 2.5 s per step. Phase identification was conducted by comparison with JCPDS database cards. From the XRD data, the degree of crystallinity of the synthesised HAP was estimated using the following Eq. (1) [42]:

$$d_c = \left(\frac{K}{B_{(002)}}\right)^3 \quad (1)$$

where d_c is the degree of crystallinity, B_{002} is full width at half maximum (°) of reflection (002) and K is a characteristic constant for HAP structures found equal to 0.24. Moreover, the Co_3O_4 crystallite size was calculated by Scherrer equation, using Co_3O_4 (311) (2θ = 37.1°) diffraction line broadening.

Fourier transform infrared spectroscopy (FTIR) absorption spectra were recorded in the 400–4000 cm^{-1} range with a Cary 600 Series FTIR spectrometer using disks of samples diluted in KBr. The oxidation states and the coordination of Co were evaluated by diffuse reflectance UV–vis spectroscopy (UV–vis-NIR DRS) with a UV–vis-NIR Cary 5000 apparatus coupled to Diffuse Reflectance Internal 2500 within a range of 200–2500 nm.

XPS spectra were recorded on a Phoibos 150 1D-DLD analysis system from Specs, with monochromatic Al Kα radiation (1486.6 eV). The hemispheric photoelectron analyser worked with a pass energy of 40 eV for survey scan and 20 eV for detail scan.

Transmission electron microscopy (TEM) observations were carried out with a Philips CM200 transmission electron microscope equipped with LaB_6 filament operating at 200 kV. The sample powder was dispersed in ethanol, dropped on copper grids, coated with lacey carbon film, and evaporated at room temperature.

Redox behaviour was examined by temperature-programmed reduction (H_2-TPR) on a Micromeritics AutoChem 2920 instrument. Firstly, all the samples were pre-treated in an oxygen stream (5%O_2/He) at 400 °C for 1 h and then cooled to room temperature. The reducing gas used in all experiments was 5%H_2/Ar, with a flow rate of 50 cm^3 min^{-1}. The temperature range explored was from room temperature to 1000 °C, with a heating rate of 10 °C min^{-1}. This temperature was maintained for 30 min. The water produced by reduction was trapped in a cold trap, and the consumption of

H_2 was quantitatively measured by time integration of the TPR profiles.

The acid/base properties of the catalysts were determined by NH_3-pulse/CO_2-pulse experiments carried out at 120 °C. The samples were submitted to a pre-treatment routine consisting of heating in a flow of 5%O_2/He, at 500 °C (30 min), and cooling down to 120 °C in a flow of He. NH_3 or CO_2 pulses were then injected in a He carrier over the sample during 30 s, with a time interval between pulses of 10 min. The NH_3 or CO_2 signal was online analysed online with an automatic apparatus Micromeritics, AutoChem 2920 instrument, equipped with thermal conductivity detector (TCD).

2.3. Catalytic tests

Catalytic tests were performed in a bench-scale fixed bed reactor operated at atmospheric pressure. The reactor was made of quartz with an internal diameter of 10 mm and a height of 300 mm, in which the temperature is controlled with a thermocouple placed in the catalyst bed. Typically 0.85 g of catalyst in powdered form (0.3–0.5 mm) was loaded. The reaction feed consisted of 1000 ppm of DCE in dry air with a total gas flow of 500 $cm^3\ min^{-1}$ (15,000 h^{-1}). It should be noted that the experimental conditions employed in this work were chosen to meet the criteria to ensure the absence of the mass and heat transfer limitations, as described elsewhere [11]. Catalytic activity was measured over the range 150–500 °C and conversion data were calculated by the difference between inlet and outlet concentrations. Conversion measurements and product profiles were taken at steady state, typically after 30 min on stream.

The feed and effluent streams were analysed using an on-line 7980A Agilent Technologies gas chromatograph equipped with a thermal conductivity (CO and CO_2) and an electron capture detector (chlorinated hydrocarbons). Analysis of HCl and Cl_2 was carried out by means of ion selective electrode and titration, respectively. Further details on analytical procedures can be found elsewhere [11]. On basis of the concentrations [Ci] at the outlet of the reactor, product yields (CO_2, CO, vinyl chloride (VC: C_2H_3Cl), HCl and Cl_2) were calculated, according to the following equations:

$$S_{CO_2} = \frac{[CO_2]}{2[VC]+[CO_2]+[CO]} \quad (2)$$

$$S_{CO} = \frac{[CO]}{2[VC]+[CO_2]+[CO]} \quad (3)$$

$$S_{VC} = \frac{2[VC]}{2[VC]+[CO_2]+[CO]} \quad (4)$$

$$S_{HCl} = \frac{[HCl]}{2[Cl_2]+[CV]+[HCl]} \quad (5)$$

$$S_{Cl_2} = \frac{2[Cl_2]}{2[Cl_2]+[CV]+[HCl]} \quad (6)$$

3. Results and discussion

3.1. Characterisation of the samples

3.1.1. Chemical analysis

Table 1 shows the chemical composition of the HAP-supported cobalt catalyst along with that of the bare support. Judging from the obtained results, the synthesised support consists of a calcium-deficient hydroxyapatite with Ca/P molar ratio equal to 1.50, lower than the 1.67 expected for a stoichiometric hydroxyapatite ($Ca_{10}(PO_4)_6(OH)_2$). According to many authors this non-stoichiometry can be explained by loss of Ca^{2+} ions, which is corrected by insertion of H^+ ions at the expense of hydroxyl groups to ensure electroneutrality [43,44]. Hence, the general formula of these calcium deficient hydroxyapatite can be denoted as

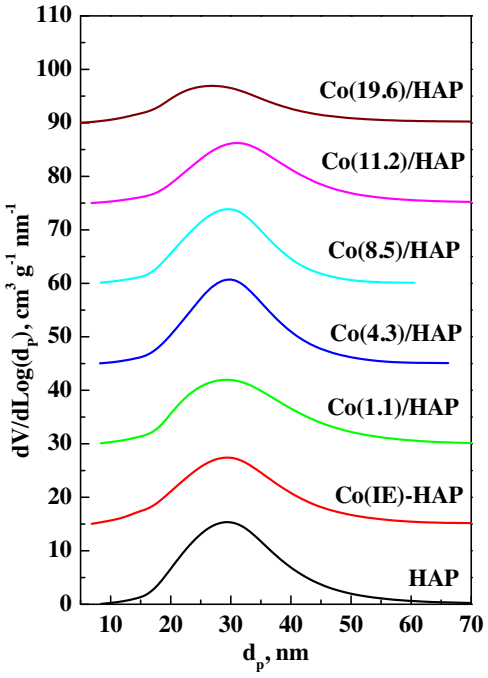

Fig 1. Mesoporous size distribution for the Co(IE)-HAP and Co(x)/HAP catalysts.

$Ca_{10-z}(HPO_4)_z(PO4)_{6-z}(OH)_{2-z}$ were $0 < z \leq 1$. The Ca/P ratio corresponding to Co(IE)-HAP sample, prepared by ion-exchange method, is relatively lower (1.20), thereby suggesting that the substituted Ca^{2+} ions were lixiviated during the filtration process. By contrast, for the five impregnated Co(x)/HAP samples, the Ca/P ratio is quite similar (about 1.5) which evidenced no further loss of calcium. On the other hand, the cobalt loadings are found to be ranged between 1.1–19.6 wt.% (Table 1). This wide range could allow us to study the evolution of the samples properties, with the progressive increase of Co surface density, from sub-monolayer to over-monolayer densities. Note that the theoretical monolayer estimation (corresponding to a cobalt loading of 8.1 wt.%) is made in accordance with that proposed for the monolayer of cobalt supported on alumina as to reach a surface density of 16Co atoms nm^{-2} [45].

3.1.2. N_2-physorption (BET measurements)

The experimental N_2 physisorption isotherms for Co(x)/HAP and Co(IE)-HAP catalysts (not shown) and the data reported in Table 1 show that the isotherms were characteristic of mesoporous materials exhibiting IV-type according to the IUPAC classification. Fig. 1 shows the pore size distributions for all the prepared catalysts. The pore size distribution corresponding to HAP support and the Co(x)/HAP catalysts ($x \leq 11.2$ wt.%) show a broad unimodal distribution centred at approximately 30 nm (Fig. 1). However, at high Co loading (19.6 wt.%) a slight shift of the distribution peak towards lower values (25 nm) is observed. On the other hand, the increased addition of cobalt to HAP produces a progressive drop in its specific surface area (up to 25%) and pore volume (up to 39%). For instance, the specific surface area of the resultant catalysts significantly decreases from 55 $m^2\ g^{-1}$ for the HAP bare support to 41 $m^2\ g^{-1}$ for Co(11.2)/HAP and Co(19.6)/HAP catalysts.

3.1.3. X-ray diffraction (XRD)

The Co(x)/HAP catalysts were characterised by means of X-ray powder diffraction in order to investigate their structural properties. The diffractogram of the HAP support calcined at 500 °C, Fig. 2A, is identical to the hexagonal hydroxyapatite structure presenting a

Table 1
Characterization of the Co(x)/HAP catalysts (fresh and used in the DCE oxidation).

Catalysts	Fresh samples								Used samples			
	Ca,[a] wt.%	P,[a] wt.%	Ca/P	Co,[a] wt.%	S_{BET}, $m^2\ g^{-1}$	Vp, $cm^3\ g^{-1}$	d_p, nm	Co_3O_4, nm[b]	S_{BET}, $m^2\ g^{-1}$	Vp, $cm^3\ g^{-1}$	d_p, nm	Co_3O_4, nm[b]
HAP	33.4	17.2	1.50	0.0	55	0.41	25.8	–	44	0.39	25.9	–
Co(IE)-HAP	29.9	19.6	1.20	1.1	57	0.38	23.4	–	42	0.30	22.5	–
Co(1.1)/HAP	40.5	20.3	1.54	1.1	53	0.39	25.2	–	35	0.23	18.8	–
Co(4.3)/HAP	36.6	18.7	1.51	4.3	46	0.36	25.5	28	43	0.27	20.0	23
Co(8.5)/HAP	29.5	16.3	1.40	8.5	45	0.34	24.6	23	36	0.23	20.5	32
Co(11.2)/HAP	27.3	14.8	1.43	11.2	41	0.32	26.8	25	39	0.26	21.1	28
Co(19.6)/HAP	29.6	15.4	1.48	19.6	41	0.25	21.3	20	29	0.27	26.4	23

[a] Determined by ICP.
[b] Co_3O_4 particle size as determined by XRD.

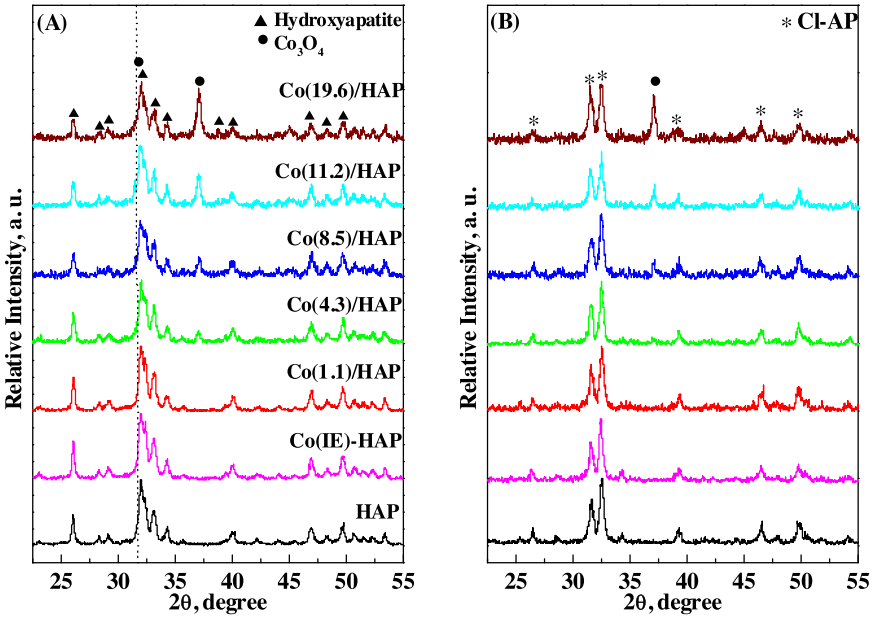

Fig. 2. XRD patterns of the Co(IE)-HAP and Co(x)/HAP: (A) fresh catalysts and (B) catalysts used in DCE oxidation.

$P6_3/m$ space group (JCPDS: 74-0565). Moreover, the degree of crystallinity of the prepared HAP is estimated to be around 0.8. This is in agreement with an earlier study reporting that the calcination of apatite materials at or above 500 °C could lead to a crystallinity degree of about 0.7–0.8 [46]. It should be pointed out that the presence of hydroxyapatite as unique phase, on the HAP diffractogram, confirms that its structure is tolerant to deviation from the stoichiometry. Yet, the formation of β-tricalcium phosphate as a product of hydroxyapatite decomposition is not expected after calcination at 500 °C [44].

The diffractograms of Co(IE)-HAP and Co(1.1)/HAP catalysts show no lines corresponding to cobalt oxides crystals (Fig. 2A) probably because of their high dispersion and/or the fact that the formed crystallites are smaller than their detection limit. With these limitations spectroscopic measurements could present an alternative option to characterise these samples because well-resolved spectra could be obtained with small Co loadings. At higher Co concentration, 4.3–19.6%, two additional typical peaks belonging to Co_3O_4 spinel structure, JCPDS 76-1802, appeared at $2\theta = 31.6°$ and 37.1° (Fig. 2A). Their intensity increases, as expected, with cobalt loading. Table 1 also reports the Co_3O_4 crystal size calculated by Scherrer equation. The average size of the Co_3O_4 particles is around 24–32 nm on the Co(x)/HAP catalysts ($x \geq 4.3\%$).

3.1.4. Transmission electron microscopy (TEM)

The catalysts with low Co loadings, Co(1.1)/HAP and Co(IE)-HAP, were investigated by TEM in order to estimate the Co species particle sizes, not detected by XRD. The micrographs of the two samples show some differences in morphology (Fig. 3). On the Co(IE)-HAP catalyst some scratched dark areas and zones presenting low contrast are observed. The presence of the former may be related with well crystallised HAP areas where some of its reticular planes form channels in which the Co ions are incorporated. The measured distance between visible diffraction plans is approximately 0.8 nm (Fig. 3). Examination of Co(1.1)/HAP micrograph reveals the presence of similar areas observed on the Co(IE)-HAP catalyst together with small Co particles, ranged between 6 and 10 nm, which have a quasi spherical shape. Since the two samples are loaded with the same amount of Co, 1.1 wt.%, these observations are probably related with the method used for the preparation of each catalyst and the subsequent distribution of formed Co species. As will be shown later, the apparition of Co species with relatively high particle sizes on the impregnated sample (Co(1.1)/HAP) compared to Co(IE)-HAP, prepared by ion exchange method, may be explained by the growth of some Co species on the support surface.

3.1.5. Fourier transform infrared spectroscopy (FTIR)

FTIR spectroscopy is commonly used to complete the structural characterisation of apatite materials made by means of XRD techniques. The objective is essentially to confirm the presence of hydroxyls and phosphate groups and the presence or the absence of some derived phosphate groups like $(HPO_4)^{2-}$ anions. Fig. 4 includes the FTIR spectra for HAP and Co(x)/HAP catalysts. The recorded spectrum corresponding to HAP bare support is char-

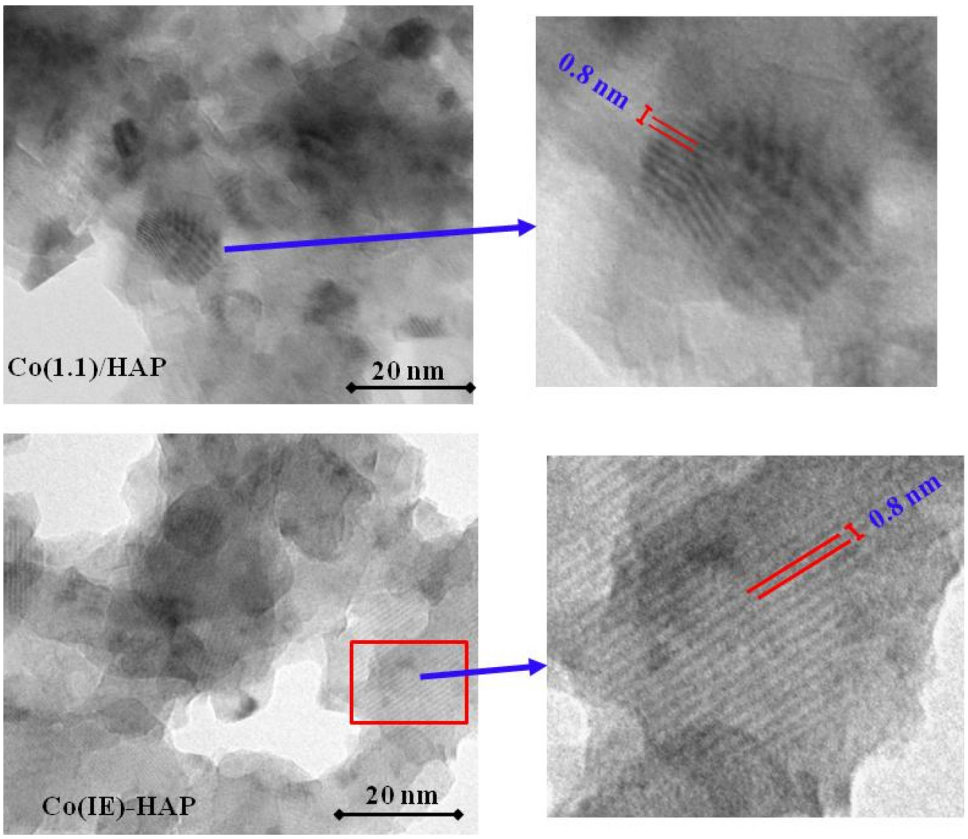

Fig. 3. (Left) TEM micrographs of Co(IE)-HAP and Co(1.1)/HAP catalysts. (Right) Highlighted visible diffraction plans.

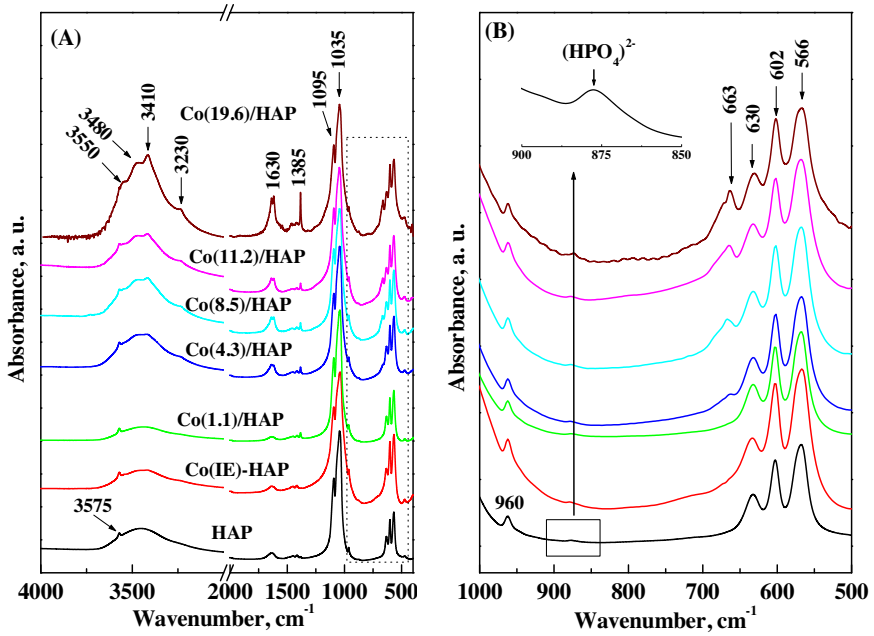

Fig. 4. FTIR spectra of Co(x)/HAP (A) 4000–400 domain and (B) 1000–500 domain.

acteristic of non-stoichiometric hydroxyapatite structures (Fig. 4). The five bands centred at 566, 602, 960, 1035 and 1095 cm^{-1} are assigned to different vibration modes of P—O bonds in the $(PO_4)^{3-}$ groups [27,28,47]. Moreover, the vibration of hydroxyls groups hosted by the apatite framework is evidenced by the presence of a small sharp band at 3575 cm^{-1} and a more intense feature at 630 cm^{-1}. It should be noted that, as expected, in agreement with the ICP results, the spectrum of HAP sample presents a band around 875 cm^{-1} which attests the presence of $(HPO_4)^{2-}$ ions; typical of calcium deficient hydroxyapatite ($Ca_{10-z}(HPO_4)_z(PO_4)_{6-z}(OH)_{2-z}$). The HAP spectrum also shows additional bands attributed to adsorbed water (1630 and 3400 cm^{-1}) and carbonates (1385 cm^{-1}) [27,28,48].

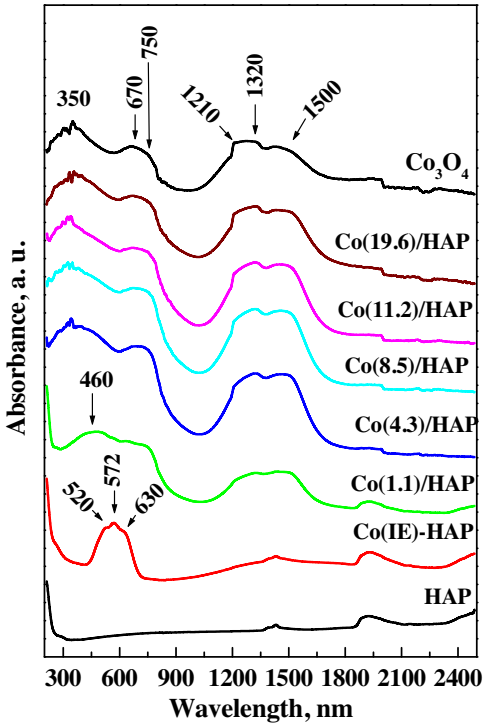

Fig. 5. UV–VIS–NIR spectra of Co(IE)-HAP and Co(x)/HAP catalysts.

It should be noted that no significant changes are detected on the Co(IE)-HAP spectrum compared with the bare support. However, the samples prepared by impregnation displayed a new band at 663 cm^{-1} which increases with the Co loading (Fig. 4). The signal is attributed to the Co—O stretching vibration characteristic of spinel Co_3O_4 [48–51]. Moreover, new shoulders appear at higher Co loading which affected the absorption of the water molecule vibrations in the 3200–3600 cm^{-1} range. Jones et al. [52] reported that this effect could indicate the presence of water coordinated to the metal ion. By contrast, at low loading the Co ion-exchanged is the dominant Co species which does not significantly disturb the vibrations of adsorbed water molecules.

3.1.6. UV–vis-NIR diffuse reflectance spectroscopy (UV–vis-NIR DRS)

Diffuse reflectance spectroscopy was used to study the symmetry and the oxidation state of cobalt species dispersed on the HAP support. It is known that, in normal Co_3O_4 spinel structure, the Co^{2+} ions ($3d^7$) occupy tetrahedral coordination (Td) while the Co^{3+} ions ($3d^6$) host an octahedral surrounding (Oh). The optical spectra of these Co species are generally composed of i) three spin allowed d–d transitions in the visible region corresponding to Co^{3+} Oh symmetry and ii) three transitions in the visible and NIR regions for the Co^{2+} Td coordination. Moreover, the interaction between the two Co sites can produce additional absorption bands due to metal to metal charge transfer distributed between the visible and NIR regions.

Fig. 5 displays the UV–vis-NIR spectra for the prepared Co(x)/HAP samples. A spectrum of bulk Co_3O_4, prepared by decomposition of cobalt nitrate at 500 °C, is also analysed for comparison. The HAP spectrum exhibits absorption bands in the NIR region related to surface hydroxyls groups, 1300–1500 nm, and another one assigned to structural OH groups, 1900–2100 nm (Fig. 5) [27,28]. In the UV region, a band around 200 nm, ascribed to $O^{2-} \rightarrow Ca^{2+}$ charge transfers [27,28], is also observed.

The spectrum of the ion-exchanged sample, Co(IE)-HAP, is characterised by the presence of three d–d transitions bands between 520 and 630 nm, in the visible region, and a broad band extended in the NIR domain (1000–1800 nm) (Fig. 5). Similar spectra were obtained in previous works dealing with the characterisation of cobalt at cation exchange sites. For instance, in their study on spectroscopy and coordination chemistry of cobalt in molecular sieves Verberckmoes et al. [53] reported that these absorptions could be assigned to ν_3 ($^4T_{1g}(F) \rightarrow {}^4T_{1g}(P)$) and ν_1 ($^4T_{1g}(F) \rightarrow {}^4T_{2g}(F)$) transitions of the octahedral Co^{2+} located in cation exchange sites. From these results we can conclude that, in Co(IE)-HAP sample, the exchanged Co^{2+} species are probably hosted by octahedral sites.

On the other hand, the impregnated samples spectra show a striking similarity with the bulk Co_3O_4 spectrum (Fig. 5). The absorption bands centred at 1200–1500 nm and 670 nm are attributed to ν_1 ($^4A_2 \rightarrow {}^4T_1(F)$) and ν_2 ($^4A_2 \rightarrow {}^4T_1(P)$) transitions, respectively, which correspond to tetrahedral Co^{2+} [54]. Likewise, the presence of octahedral Co^{3+} ions is evidenced by their characteristic d–d transitions bands, centred at 750 nm and 350–460 nm, associated with ν_1 ($^1A_{1g} \rightarrow {}^1T_{1g}$) and ν_2 ($^1A_{1g} \rightarrow {}^1T_{2g}$), respectively [54]. It is relevant to highlight that the latter shifts towards the UV domain with Co loading (from 460 nm for Co(1.1)/HAP to 350 nm for the catalysts with higher Co loading). This suggests the growth of tridimensional and well crystallised Co_3O_4 on these Co-rich samples. By contrast, despite the presence of Co^{3+} and Co^{2+} ions on the Co(1.1)/HAP sample its spectrum shows a difference respect to those corresponding to Co($4.5 \leq x \leq 19.6$)/HAP. Moreover, it was observed that the color turned from grey for the Co(1.1)/HAP to black for the Co($4.5 \leq x \leq 19.6$)/HAP catalysts. According to earlier studies [55], these observations clearly indicate that on the Co(1.1)/HAP catalyst the Co could form Co_xO_y clusters composed of a mixture of octahedral Co^{3+} and tetrahedral Co^{2+}. These can be considered as precursors of Co_3O_4 nanocrystals. These results are in agreement with the findings from TEM and XRD analyses. The Co species particles (< 10 nm) found on the Co(1.1)/HAP are much smaller than those corresponding to Co($4.5 \leq x \leq 19.6$)/HAP catalysts, in the 23–32 nm range. It is worth mentioning that the presence of exchanged Co^{2+} species in the impregnated Co(x)/HAP samples can not be ruled out since their absorption bands may overlap with those of spinel Co_3O_4 structure.

3.1.7. X-ray photoelectron spectroscopy (XPS)

The influence of the Co content on the surface distribution of cobalt species has been investigated by means of XPS techniques. Fig. 6 and Table 2 summarise the corresponding results. The Co 2p XPS spectra for all the Co(x)/HAP samples have been processed while maintaining the Co $2p_{3/2}$/Co $2p_{1/2}$ area ratio at approximately 2 (Fig. 6). The Co $2p_{3/2}$ spectra consist of a main photoemission peak (M) located at a binding energy (BE) in the range of 780.8–783 eV and a satellite peak (S) attributed to a shake-up process, appearing at approximately 6–8 eV higher BE.

In the Co $2p_{3/2}$ region, the XPS profile for the Co(IE)-HAP catalyst exhibits two peaks, centred at 783.1 and 788.9 eV, attributed to Co^{2+} and its typical shake-up satellite peak, respectively. As expected, the impregnation of cobalt onto the HAP surface slightly shifts the Co $2p_{3/2}$ main peak position to lower BE, compared to Co(IE)-HAP sample, suggesting the near surface enrichment with Co^{3+} ions (Fig. 6 and Table 2) [54]. The main Co $2p_{3/2}$ peak corresponding to Co(8.5)/HAP, Co(11.2)/HAP and Co(19.6)/HAP tend to split into two signals corresponding to two distinct contributions. The first one centred at 780.8 eV is attributed to Co^{3+} ions while the shoulder situated at 783.2 ± 0.2 eV is assigned to Co^{2+} species. These results are in good agreement with the FTIR and DRS studies and clearly corroborated the previous findings by evidencing the formation of Co_3O_4 crystals in the impregnated Co($x \geq 4.3$)/HAP samples. This conclusion is also supported by the spin-orbit splitting (ΔE) and S/M ratio values reported in Table 2. Indeed, the observed decrease in these two parameters with increasing Co content suggests the

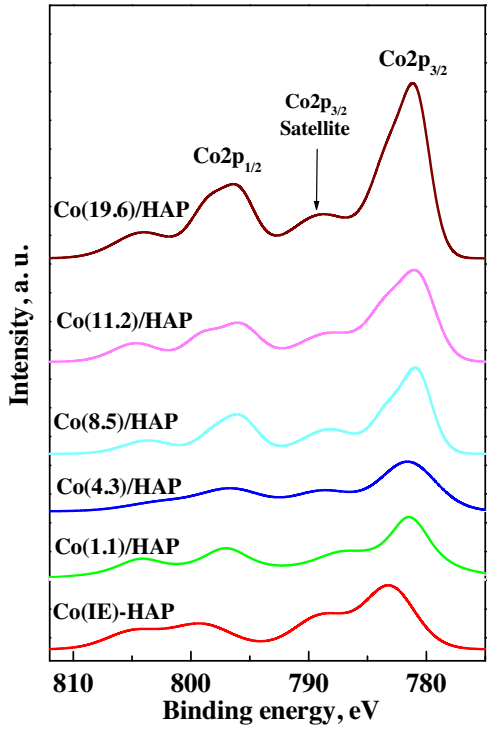

Fig. 6. XPS spectra of Co $2p_{3/2}$ – Co $2p_{3/2}$ region for Co(IE)-HAP and Co(x)/HAP catalysts.

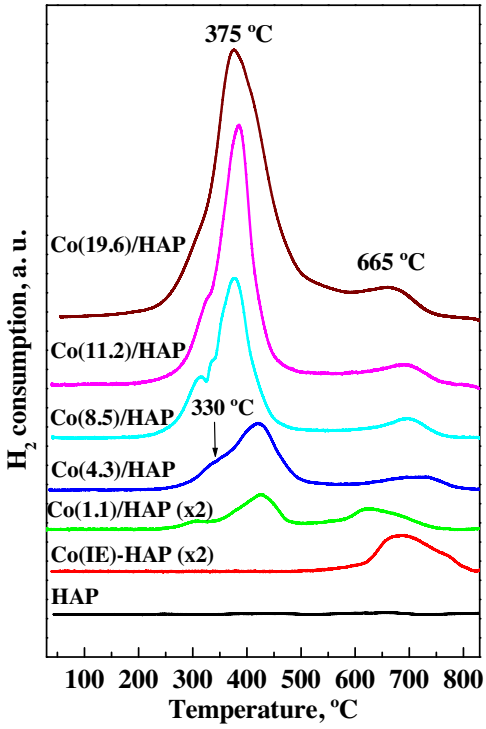

Fig. 7. H_2-TPR profiles of Co(IE)-HAP and Co(x)/HAP catalysts.

evolution towards a major contribution of Co^{3+} ions and, then, the deposition of spinel Co_3O_4 structure [54]. For instance, the measured ΔE decreases from 16.4 eV for Co(IE)-HAP catalyst to 15 eV for Co(8.5)/HAP Co(11.2)/HAP and Co(19.6)/HAP catalysts. Likewise, the calculated S/M values decrease from 0.60 for Co(IE)-HAP to 0.39 for Co(11.2)/HAP and Co(19.6)/HAP catalysts.

Table 2 also offers a comparison between the Co/Ca molar ratios calculated from the XPS and ICP data. When comparing the Co/Ca molar ratio values of Co(IE)-HAP and Co(1.1)/HAP catalysts, having the same Co content (1.1 wt.%) but prepared by different methods, it is observed that it is higher in the ion-exchanged sample. This higher Co/Ca ratio value can be explained by the substitution of Ca^{2+} ions lixiviated during the filtration process, by Co^{2+} ions.

3.1.8. Temperature programmed reduction (H_2-TPR)

The H_2-TPR experiments were performed in order to investigate the reducibility of different Co species present in the Co(x)/HAP and Co(IE)-HAP catalysts. To our knowledge, similar H_2-TPR study, concerning the Co/HAP materials, has not been yet published. Fig. 7 displays the H_2-TPR profiles of Co(IE)-HAP and Co(x)/HAP for different Co loadings. Table 3 reports the quantitative data calculated from the integration of the resulted reduction peaks. Fig. 7 shows that no reduction peak was found on the HAP bare support. The diagram of Co(IE)-HAP sample shows a broad reduction peak at high temperature (>500 °C), associated with the reduction of exchanged Co^{2+} ions. As shown in Table 3, the integration of this reduction peak gives a value of H_2 consumption of 0.29 mmol g^{-1} (1.14% Co^{2+}). This is consistent with our above mentioned proposal (the presence of exchanged Co^{2+} as unique Co phase) since it was close to the overall Co content (1.1%) determined by ICP.

Fig. 7 also shows the H_2-TPR traces corresponding to Co(x)/HAP impregnated catalysts. In this series of catalysts, the reduction profiles are quite similar. Hence, they are characterised by the presence of two typical reduction peaks of bulk Co_3O_4, in the 250–500 °C temperature range, and a reduction peak due to the exchanged Co^{2+} ions at high temperatures (>500 °C). The Co_3O_4 reduction process takes place realised through two steps consisting of the reduction of Co^{3+} ions to Co^{2+} (peak around 300–330 °C) accompanied by much more intense reduction peak due to the reduction of Co^{2+} ions to metallic cobalt (375–430 °C) [11]. As revealed by the sixth column data reported in Table 3, the H_2/Co molar ratio values (1.4–1.5) corresponding to the low reduction peaks temperatures (<500 °C) for Co(8.5 ≤ x ≤ 19.6)/HAP catalysts are close to 1.33, expected for

Table 2
XPS study of the Co(x)/HAP catalysts (fresh and used in the DCE oxidation).

Catalysts	Fresh catalysts						Used catalysts		
	Co $2p_{3/2}$, eV	Co $2p_{3/2}$ satellite, eV	Co/Ca, % (XPS)	Co/Ca, %(ICP)	ΔE,eV[a]	S/M[b]	Co $2p_{3/2}$ BE, eV	C, wt.%	Cl, wt.%
HAP	–	–	0.0	0.0	–	–	–	0	6.8
Co(IE)-HAP	782.9	788.9	8.9	1.8	16.4	0.60	782.7	3.0	7.6
Co(1.1)/HAP	781.8	787.6	3.6	1.9	16.0	0.43	782.3	1.8	8.4
Co(4.3)/HAP	780.9	788.7	6.8	8.0	15.0	0.44	782.7	0	9.6
Co(8.5)/HAP	780.6	788.2	9.4	19.6	15.0	0.38	780.9	0	10.0
Co(11.2)/HAP	781.5	788.3	14.9	27.9	15.0	0.39	781.6	0	10.2
Co(19.6)/HAP	781.5	788.8	15.7	45.0	15.0	0.39	781.3	0	9.8

[a] Spin-orbit coupling calculated as: ΔE = Co $2p_{1/2}$ – Co $2p_{3/2}$.
[b] Co $2p_{3/2}$ satellite intensity relative to main photoelectron line.

Table 3
Reducibility and surface chemistry of the prepared Co(x)/HAP catalysts.

Catalysts	H_2-TPR data					Volumetric adsorption studies at 120 °C			
	H_2 uptake, mmol g^{-1}	H_2/Co	H_2 uptake, mmol g^{-1} (>500 °C)[a]	IE Co, wt.%[b]	H_2/Co[c] (<500 °C)	Ads NH_3, μmol g^{-1}	Ads NH_3, μmol m^{-2}	Ads CO_2, μmol g^{-1}	Ads CO_2, μmol m^{-2}
HAP	0	0	0	0	0	80	1.45	12	0.22
Co(IE)-HAP	0.29	1.5	0.29	1.14	0	110	1.93	6	0.11
Co(1.1)/HAP	0.42	2.3	0.17	0.67	3.4	120	2.26	25	0.47
Co(4.3)/HAP	1.19	1.6	0.24	0.94	1.7	100	2.17	25	0.54
Co(8.5)/HAP	2.02	1.4	0.30	1.18	1.4	50	1.11	22	0.49
Co(11.2)/HAP	2.86	1.5	0.34	1.34	1.5	32	0.78	18	0.45
Co(19.6)/HAP	4.68	1.4	0.35	1.37	1.4	40	0.98	20	0.49

[a] Integration of reduction peak at T> 500 °C.
[b] Ion-exchanged Co amount reducible at T> 500 °C as determined from H_2-TPR data.
[c] H_2/Co molar ratio corresponding to the reduction peaks at T < 500 °C.

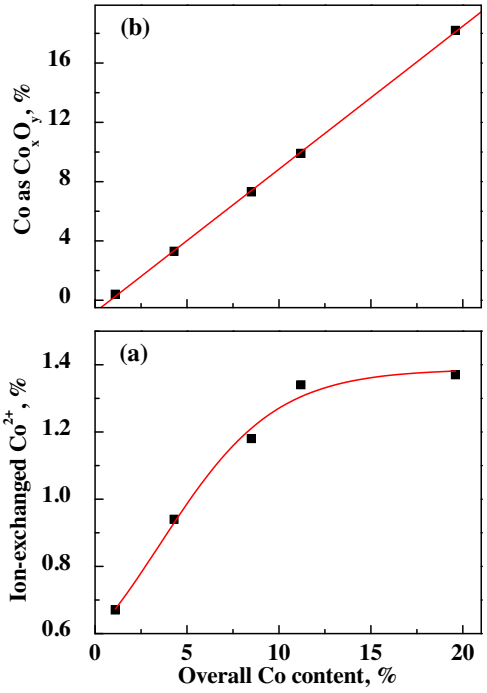

Fig. 8. Amounts of (a) exchanged cobalt and (b) Co forming Co_3O_4 or Co_xO_y phase on the Co(x)/HAP catalysts, as determined by H_2-TPR, versus overall Co content.

stoichiometric Co_3O_4. By contrast, for the Co(1.1)/HAP sample this value is significantly higher (3.4) suggesting the deposition of non-stoichiometric Co_3O_4. The latter is in good agreement with our characterisation results, discussed above, which suggested the formation of Co_xO_y clusters composed of a mixture of octahedral Co^{3+} and tetrahedral Co^{2+}. Fig. 8 reports the relationship between the overall Co content determined by ICP and the contribution of the two phases of Co, ion-exchanged and deposited as Co_3O_4 or Co_xO_y, calculated from the integration of the corresponding reduction peaks. The amount of Co ion-exchanged species increases slowly with the Co loading from 0.67% on Co(1.1)/HAP up to 1.34%, on the Co(11.2)/HAP catalyst, above which remains unchanged with Co loading. However, the contribution of Co spread as Co_3O_4 or Co_xO_y over the carrier linearly increases with Co loading.

3.1.9. Volumetric adsorption studies

The acid-base properties of the prepared catalysts were investigated by means of volumetric adsorption techniques. NH_3 and CO_2 were used as probe molecules to determine the acid and basic surface densities, respectively. Twenty consecutive pulses at 120 °C separated by 10 min evacuation treatment at the same temperature were recorded. In general, the first pulses of reactive gas are sufficient to reach the maximum adsorption capacity of the samples. Then, the adsorption data are determined from the difference between the first and second experimental pulses. The corresponding data are included in Table 3.

Hence, the surface density for NH_3 adsorption sites on HAP support is 1.45 μmol m^{-2} whereas it does not adsorb more than 0.22 μmol m^{-2} of CO_2. This difference is explained by the calcium deficiency of the support which leads to a surface with a notable acidic character [27,28]. This is why in the case of the Co(IE)-HAP sample, presenting a substitution of Ca^{2+} by Co^{2+} ions, the density of surface acidity is, even more, enhanced (1.93 μmol m^{-2}) at the expense of the surface basicity (0.11 μmol m^{-2}).

Though not proceeding via analogous pathway the impregnation of cobalt onto the HAP surface influences dramatically the amount of the adsorbed NH_3 and CO_2. According to Table 3, the surface density of adsorbed CO_2 on the support, 0.22 μmol m^{-2}, is much smaller than that determined for Co(x)/HAP, 0.45–0.54 μmol m^{-2}. Likewise, the surface acidity slightly increases with the addition of small amounts of Co (≤4.3%), but it notably decreases for the samples with high Co loadings (≥8.5%). For example the surface density of adsorbed NH_3 results in 2.26 μmol m^{-2} for Co(1.1)/HAP while around 1.11 μmol m^{-2} in the case of the Co(8.5)/HAP catalyst. This drastic change in the acid character on the Co(x)/HAP catalysts can be explained by the achievement of Co monolayer densities which cover totally the support surface and, then, minimise their surface acidity. However, for all the Co(x)/HAP catalysts, the surface basicity becomes twice compared to bare HAP support.

3.2. Catalytic behaviour in the oxidation of 1,2-dichloroethane (DCE)

The DCE oxidation reaction was examined over the calcined catalysts in the temperature window between 150 and 500 °C, by sequentially increasing the reaction temperature with 25 °C intervals (light-off curves). Fig. 9A displays the evolution of DCE conversion (X_{DCE}) over the Co(x)/HAP catalysts versus reaction temperature. With the reactor filled up with pure HAP the reaction begins around 200 °C and increased slowly up to 300 °C. Then it started to increase rapidly with reaction temperature. At 450 °C, the DCE conversion is close to 100%. Over the Co(IE)-HAP ion-exchanged catalyst the reaction ignition starts at 275 °C and the conversion increases slowly with the temperature, but it does not exceed 83% at 500 °C. The shape of activity traces for Co(x)/HAP impregnated catalysts is almost similar compared to

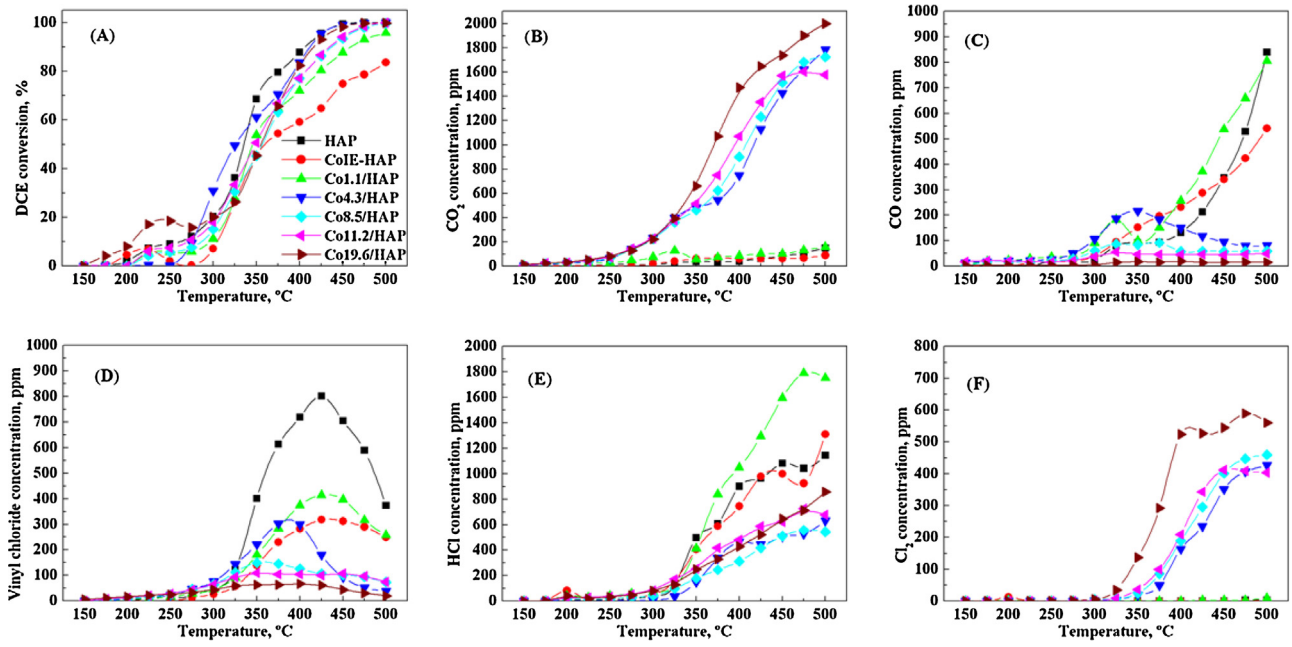

Fig. 9. DCE conversion and products distribution on the Co(IE)-HAP and Co(x)/HAP catalysts.

Table 4
Catalytic data in DCE oxidation over Co(x)/HAP samples.

	T_{10}, °C	T_{50}, °C	T_{90}, °C	Carbon balance, %[a]	CO/CO_2[a]	Cl_2/HCl[a]	$mol_{DCE}\ g_{cata}^{-1}\ s^{-1}$ ($\times 10^8$)[b]	$mol_{DCE}\ m^{-2}\ s^{-1}$ ($\times 10^{10}$)[b]	Ea[c], kJ mol^{-1}
HAP	255	335	406	87	5.60	0.002	1.3	2.40	105 ± 1.8
Co(IE)-HAP.	303	360	–	72	6.00	0.002	0.4	0.77	108 ± 1.3
Co(1.1)/HAP	293	345	460	78	5.10	0.005	2.1	3.90	75.7 ± 0.7
Co(4.3)/HAP	275	325	413	97	0.05	0.676	3.0	6.60	66.4 ± 0.7
Co(8.5)/HAP	282	355	438	97	0.03	0.845	3.0	6.80	60.7 ± 0.1
Co(11.2)/HAP	275	349	435	89	0.03	0.596	3.0	7.20	62.0 ± 0.3
Co(19.6)/HAP	205	355	417	103	0.01	0.653	2.9	7.10	58.0 ± 0.4
Co_3O_4 [59]	285	380	465	–	–	–	2.6	0.24	55.3 ± 0.4

[a] Values calculated at 500 °C.
[b] Reaction rate calculated at 250 °C.
[c] Activation energy.

that of HAP support. Table 4 compares the obtained results in terms of temperatures at which the DCE conversion reached 10 (T_{10}), 50 (T_{50}), and 90% (T_{90}). Some recently published results for a bulk Co_3O_4 oxide (11 $m^2\ g^{-1}$) are used as reference for comparison [59]. Data in Table 4 show that the catalytic activity, on the basis of T_{50} values, follows this trend: Co(4.3)/HAP (325 °C) > HAP (335 °C) > Co(1.1)/HAP (345 °C) > Co(11.2)/HAP > Co(8.5)/HAP∼ Co(19.6)/HAP > Co(IE)-HAP (360 °C) > Co_3O_4 (380 °C). This tendency proves the comparable potential of HAP support in comparison with the cobalt catalysts to decompose DCE. Table 4 also shows activity data referred to 1 g of catalyst and 1 m^2 of BET surface area. On the HAP sample the specific catalytic activity is around $2.4 \times 10^{-10}\ mol_{DCE}\ m^{-2}\ s^{-1}$ suggesting that Ca-deficient hydroxypatite is not an inert support when applied in DCE oxidation reaction. For the series of Co(x)/HAP impregnated catalysts the specific catalytic activity value seems to increase with the cobalt loading from 3.9×10^{-10} for Co(1.1)/HAP to $7.1 \times 10^{-10}\ mol_{DCE}\ m^{-2}\ s^{-1}$ for Co(11.2)/HAP catalyst but it remains almost constant for the catalyst with the highest copper loading (19.6%). It is worth outlining that the Co(IE)-HAP catalyst shows the lowest activity ($0.8 \times 10^{-10}\ mol_{DCE}\ m^{-2}\ s^{-1}$) with respect to the Co(x)/HAP catalysts. Besides, when compared to the low specific activity of pure Co_3O_4 ($0.24 \times 10^{-10}\ mol_{DCE}\ m^{-2}\ s^{-1}$) the notable improved textural and structural properties of the resulting Co/hydroxyapatite catalysts make them advantageously more active than the bulk spinel.

Table 4 summarises the values of the apparent activation energy (Ea) for the Co(x)/HAP catalysts. The corresponding calculations are made assuming a first order reaction and a linear correlation is obtained between ln[-ln(1-X_{DCE})] and 1/T (Fig. 10). The analysis of the obtained results shows that relatively high activation energy values, 105–108 kJ mol^{-1}, are obtained on the HAP and Co(IE)-HAP catalysts. However, the Ea values decrease significantly with the supported cobalt phases to reach values about 58–62 kJ mol^{-1} over Co($x \geq 8.3\%$), close to those exhibited by the bulk Co_3O_4 prepared by different routes (53–56 kJ mol^{-1}) [59].

3.3. Structure-activity-selectivity relationships

In their study on the methanol oxidation reaction over Co/hydroxyapatite Aellach et al. [37] concluded that the redox properties of Co_3O_4 and acid properties of the apatite support led to a very efficient catalyst compared to bulk Co_3O_4. Moreover, the presence of surface cationic vacancies on the Ca-deficient hydroxyapatite can improve the catalytic activity. This might explain the low activity of our Co(IE)-HAP catalyst. The characterization of the

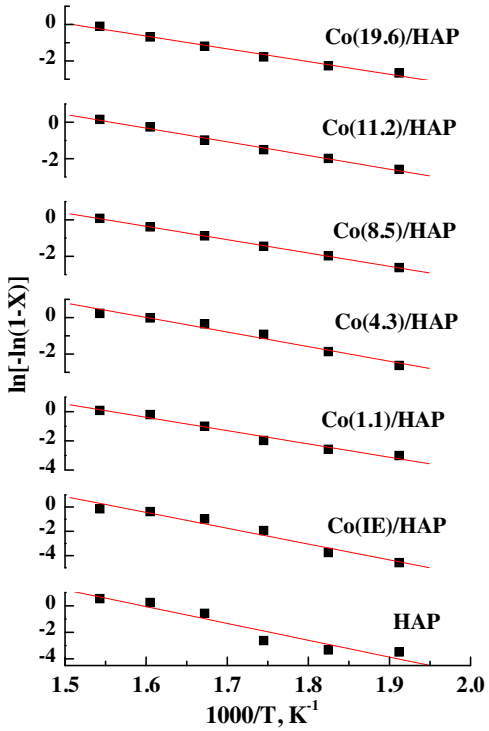

Fig. 10. Pseudo-first order fit for the DCE oxidation experimental data over the Co(x)/HAP catalysts.

latter has confirmed the presence of hardly reducible Co^{2+} (ion-exchanged) as unique Co phase. Then, the poor performance can be related to an inactivity of this Co species and the absence of surface cationic vacancies which are occupied by the Co^{2+} ions. The relatively higher activity of HAP, compared to that of Co(IE)-HAP, can support our claim; especially, the former contains cation vacancies due to its Ca-deficiency.

On the other hand, the increase of the activity over the Co(x)/HAP samples with the increase of Co loadings can be explained by the surface Co_3O_4 enrichment which contains easily reducible Co^{3+} and Co^{2+} species. This is in good agreement with the relatively comparable activation energy determined on the Co-rich samples and bulk Co_3O_4 (Table 4). This suggests that the activity is controlled by similar near surface composition, characterised by an abundance of Co_3O_4 crystals. On pure Co_3O_4 the surface density of Co sites is certainly larger than that for Co(x)/HAP supported samples; however, this difference is overcompensated by their much higher surface area and their relatively low Co_3O_4 crystal size (20–25 nm) compared with bulk Co_3O_4 (38 nm).

Fig. 9 (B–F) show the concentration-temperature profiles of the main oxidation products (CO_2, CO, VC, HCl and Cl_2, respectively). Table 4 also includes the carbon balance, CO/CO_2 and Cl_2/HCl ratios calculated at 500 °C for each tested catalyst. The formation of CO_2, as deep DCE oxidation (7) product, seems to be affected by the Co loading and, then, the Co species lying on the surface (Fig. 9B).

$$C_2H_4Cl_2 + 5/2O_2 \rightarrow 2CO_2 + 2HCl + H_2O \quad (7)$$

For the catalysts with Co contents lower than 4.3% the CO_2 production does not exceed 100 ppm whereas it notably increased over the high Co loading catalysts ($x \geq 4.3\%$). For instance, on the Co(19.6)/HAP catalyst the CO_2 concentration reaches a maximum of 2000 ppm at 500 °C and over Co(4.3)/HAP 1700 ppm of CO_2 is produced at 500 °C. It could be concluded that, in agreement with our characterisation results, formation of CO_2 as a product of the DCE total oxidation should mainly involve the Co_3O_4 species (Co^{3+} and Co^{2+} ions) deposited on the support surface which are easily reducible as reported in H_2-TPR section. Conversely, the yield of CO is markedly favoured (Fig. 9C) on the low Co loading catalysts (HAP, Co(IE)-HAP and Co(1.1)/HAP). For instance, 800 ppm are produced over HAP and Co(1.1)/HAP catalysts at 500 °C. Indeed, on the Co(1.1)/HAP catalyst CO/CO_2 ratio is around 6 while it decreases to about 0.01 on the Co(19.6)/HAP catalyst (Table 4). In their study on the CO oxidation reaction on hydroxyapatite Matsumura et al. [35] reported that the introduction of tetrachloromethane into the feedstream in the CO oxidation process converts, at least partially, the hydroxyapatite to chlorinated apatite that suppresses the oxidation of CO to CO_2. We can conclude that the same phenomenon occurs in the case of our prepared HAP and the very low Co loadings catalysts (1.1%), leading to a large uncovered support surface, which inhibited the CO oxidation to form CO_2. By contrast, based on our characterisation results, it seems that deposited Co_3O_4 spinel phase on the catalysts surface, for Co loadings $\geq 4.3\%$, enhances notably the CO conversion to CO_2.

The HAP support effect on the distribution of the DCE oxidation products was also studied by analysing the VC intermediate production curves (Fig. 9D). In the case of HAP, Co(IE)-HAP and Co(1.1)/HAP catalysts a production peak centred at 425 °C is observed before decreasing sharply for $T \geq 425$ °C with high CO production, as above commented. VC concentration maxima result in 800 ppm with HAP, 400 ppm with Co(1.1)/HAP and 310 ppm with Co(IE)-HAP catalyst. Nevertheless, with Co(4.3)/HAP catalyst, the VC production peak was shifts to lower temperatures (375 °C with a maximum about 300 ppm) compared to the low Co loading catalysts ($x \leq 1.1\%$). Likewise, the amount of the produced VC continues to decline with Co loading when it did not exceed 55 ppm on the Co(19.6)/HAP catalyst. This suggests that the catalysts with low Co loadings and more acid sites are more selective to produce VC compound. Our NH_3 adsorption study, described above, pointed out that catalysts with $Co \leq 4.3\%$ have higher surface acid density compared to Co($8.5 \leq x \leq 19.6$)/HAP catalysts. This is in good agreement with a number of earlier studies in the literature [57,58] which reveal that acid sites may play a key role for the production of VC at mild temperatures as an intermediate molecule derived from hydrodechlorination of DCE, which should readily decompose finally to CO_x.

Fig. 9E and F show the production profiles of HCl and Cl_2, respectively. Generally, HCl is the preferred chlorinated product because it can be easily trapped by aqueous scrubbing [58]. As can be seen in Fig. 9E hydrogen chloride is the main deep DCE oxidation product over the HAP, Co(1.1)/HAP and Co(IE)-HAP catalysts. For instance, over Co(1.1)/HAP catalyst 1800 ppm of HCl are produced at 475 °C compared to 500 ppm produced over Co(8.5)/HAP and Co(19.6)/HAP catalysts. However, significant amount of molecular chlorine, Cl_2, is formed on the high Co loadings catalysts, $x \geq 4.5\%$, due to the occurrence of the Deacon reaction (reaction 8). At 475 °C, the Cl_2 concentration is about 550 ppm on Co(19.6)/HAP catalyst and 420 ppm on the Co(8.5)/HAP catalyst. Furthermore, as shown in Table 4, at 500 °C the Cl_2/HCl values are relatively higher on the Co($4.5 \leq x \leq 19.6$)/HAP catalysts (0.6–0.9). By contrast, in the case of the HAP, Co(1.1)/HAP and Co(IE)-HAP catalysts very small amounts of Cl_2 are detected in all the reaction temperatures analysed range, up to 500 °C (Cl_2/HCl = 0.002–0.005).

$$2HCl + \tfrac{1}{2}O_2 \leftrightarrow Cl_2 + H_2O \quad (8)$$

3.4. Characterisation of used catalysts

Textural, structural and surface chemistry analyses were carried out, on the spent samples, in order to study the eventual changes after reaction. The surface analysis of the used catalysts was conducted by XPS techniques, particularly focused on the determination of chlorine and carbon species deposited on the

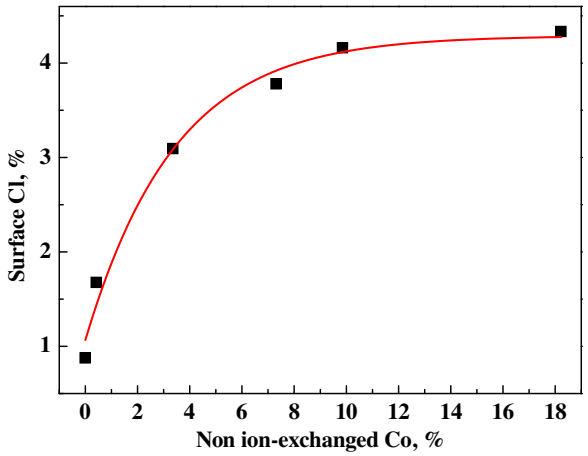

Fig. 11. Variation of the surface chlorine amounts for the tested Co(x)/HAP catalysts versus non ion-exchanged Co species amounts.

catalysts surface. According to the reported data in Table 2 the amount of accumulated chlorine on the HAP sample results in around 6.8 wt.%. This content tends to increases with Co loading up to 10 wt.% on the Co(8.5)/HAP catalyst. However, the XPS analysis shows a lower carbon deposition tendency. Indeed, carbon traces are detected on the low Co loading samples only: Co(1.1)/HAP (1.8%) and Co(IE)-HAP (3%). These results are in accordance with the lower carbon balance values found on these two tested catalysts (72% for Co(IE)-HAP and 78% for Co(1.1)/HAP), as stated in Table 4.

Irrespective of the spent catalyst, its characterisation by XRD, Fig. 2B, evidences total conversion of the hydroxyapatite into its chlorinated analogue (Cl-AP: $Ca_{10}(PO_4)_6Cl_2$). The diffractogram of this chlorinated framework is particularly characterised by two intense signals at $2\theta = 31.5^\circ$ and 32.4° (JCPDS: 027–0074). The former seems to overlap the peak, centred at 31.6°, attributed to Co_3O_4 structure. Nevertheless, the presence of the diffraction peak at $2\theta = 37.1^\circ$ proves that the spinel is still present on the spent catalysts. Similar observations concerning the phase transformation of hydroxyapatite were found in the literature [35,36]. For instance, Reichle [36] found that gaseous chlorobenzene could react with hydroxyapatite to yield chlorinated apatite. It should be noted that, although the chlorine amounts retained on the surface exceed those required to form stoichiometric Cl-AP, no additional chlorinated phases, such as cobalt(II) chloride or cobalt(II) chlorate, are detected on the spent catalysts by XRD. Nevertheless, it is known that surface cobalt oxides sites adsorb chlorine which results from the destruction of chlorinated compounds [59]. Fig. 11 depicts the effect of the non exchanged cobalt species on the resulting chlorine amount (surface Cl, %), calculated as the difference between the total chlorine amount and that required to form Cl-AP. The analysis of this figure demonstrates that the chlorine amounts increase with the surface Co species up to 4.1%, corresponding to 8.9% of non exchanged cobalt amount (close to 8.1% for theoretical Co monolayer), after which it stay almost constant. This suggests that chlorine species are adsorbed on the surface Co species.

On the other hand, the spinel Co_3O_4 ($2\theta = 37.1^\circ$) diffraction line broadening was used to estimate, by Scherrer equation, the evolution of crystallite size after catalytic test (Table 1). In this sense, no significant growth of the spinel crystallites is noticed (size estimated to be around 23–28 nm in the fresh sample while it is around 23–32 nm after catalytic test). The BET surface area of all the analysed catalysts notably decreases after reaction (Table 1). For instance, it decreases from 55 to 44 $m^2\,g^{-1}$ in the HAP sample and from 41 to 29 $m^2\,g^{-1}$ in the Co(19.6)/HAP sample. This loss of specific surface area, in all the spent catalysts, is probably due to the

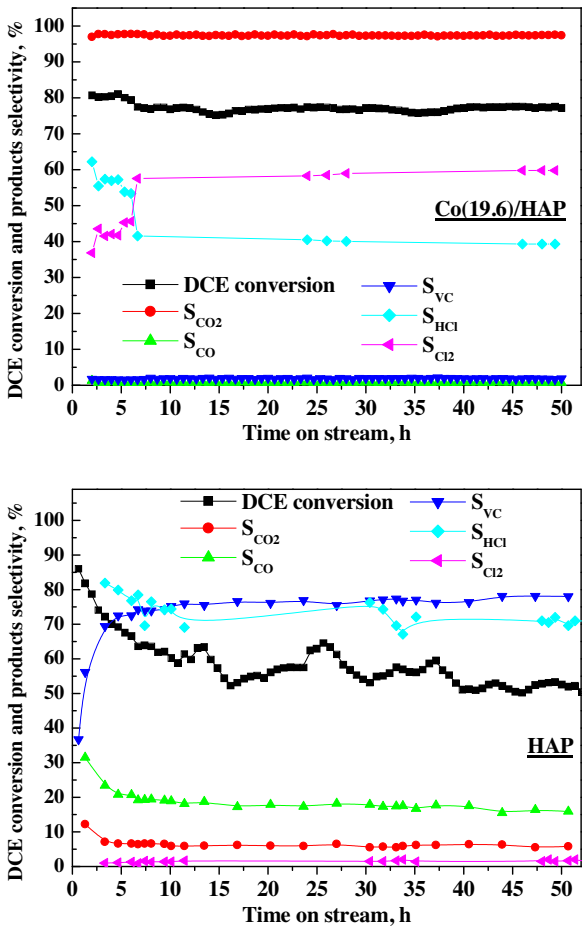

Fig. 12. DCE oxidation over HAP and Co(19.6)/HAP catalysts at 375 °C as a function of time on stream.

phase transformation of HAP support which is converted to Cl-AP [56].

3.5. Catalytic stability

The catalytic stability with time on stream of the HAP support and Co(19.6)/HAP catalysts, in the DCE oxidation process, was investigated by analysing the evolution of DCE conversion and the products selectivity with time on stream at 375 °C for 50 h (Fig. 12). In spite of a comparable activity of the two catalysts is observed at the beginning of the experiments (80–85%) the HAP suffers a significant decay with time. For instance, after 50 h HAP shows a conversion lower than 55% whereas it is still around 77% over Co(19.6)/HAP catalyst. In fact, this catalyst shows a stable performance in terms of conversion and selectivity after a reaction time interval of 7 h. The observed good stability of this sample is related to the lower impact of induced chlorination. On the basis of the observed decrease in HCl selectivity during the first seven hours, it is reasonable to think that chlorinated apatite is formed at this time interval. Afterwards stable selectivities to HCl (42%) and Cl_2(58%) are observed. Interestingly chlorination does not involve significant changes in CO_2 selectivity as it remains constant (above 98%) during the whole time span of the run.

By contrast, it seems that the HAP catalytic activity is much more affected by its structural transformation to chlorinated apatite. Moreover, the shape of the HAP activity curves versus time on stream reflects an oscillatory behaviour suggesting the intermittent regeneration of the hydroxyapatite by the produced water (Eq. (9)). Reichle [36] also observed the regeneration phenomenon of the

hydroxyapatite structure by steam in the hydrolysis of chlorobenzene. As for product distribution high VC and HCl selectivity, 76% and 70% respectively, are achieved together with significant low CO/CO_2 selectivity values (lower than 20%).

4. Conclusions

Calcium-deficient hydroxyapatite, with Ca/P ratio of 1.5, was synthesised by precipitation method. The resulted support was impregnated with cobalt and characterised by TEM, BET, XRD, FTIR, H_2-TPR, UV–vis-NIR DRS, XPS and volumetric adsorption of CO_2 and NH_3 molecules techniques. Three types of cobalt species have been identified in the impregnated Co(x)/HAP catalysts: (i) Co^{2+} ions exchanged with Ca^{2+} ions of the apatite framework, (ii) Co_xO_y clusters with small particle size (<10 nm) and (iii) well crystallised spinel Co_3O_4 structures. The volumetric adsorption study has shown that the addition of high amounts of Co (≥8.5%) notably decreases the acid character of the Co(x)/HAP catalysts surface. This is explained by the achievement of Co monolayer densities which cover totally the support surface and, thus, minimise its surface acidity. However, the addition of cobalt ($1.1 \leq x \leq 19.6$) to HAP increases by more than twice its surface basic density.

The Co(x)/HAP catalysts have been tested in the oxidation of 1,2-dichloroethane. Due to their improved textural and structural properties the resulting Co/hydroxyapatite catalysts have proved higher activity compared to bulk Co_3O_4. Moreover, the present study points out the effect of the HAP support on the catalytic stability and the distribution of the reaction products. For instance, the low Co loading catalysts have resulted more selective towards intermediate products (CO and VC). However, high stability and high selectivity to produce CO_2, as deep oxidation product, have been favoured by the Co-rich catalysts which contain the easily reducible Co^{3+} and Co^{2+} ions. The characterisation of the spent catalysts has shown that they have retained a significant amount of chlorine which consists of (i) adsorbed chlorine species on the exposed surface of bulk Co_3O_4 and (ii) a fraction that ion-exchanges hydroxide anions leading to the conversion of the hydroxyapatite into its chlorinated analogue.

Acknowledgements

The financial support for this work provided by Gobierno Vasco (GIC IT-657-13), Ministry of Economy and Competitiveness (ENE2013-41187-R) and UPV/EHU (UFI11/39) is gratefully acknowledged. Likewise, the technical support provided by SGIker (UPV/EHU) is gratefully acknowledged.

References

[1] H. Huang, Y. Xu, Q. Feng, D.Y.C. Leung, Catal. Sci. Technol. 5 (2015) 2649–2669.
[2] A. Aranzabal, B. Pereda-Ayo, M.P. González-Marcos, J.A. González-Marcos, R. López-Fonseca, J.R. González-Velasco, Chem. Pap. 68 (2014) 1169–1186.
[3] B. Huang, C. Lei, C. Wei, G. Zeng, Environ. Int. 71 (2014) 118–138.
[4] M.C. Krol, J. Lelieveld, D.E. Oram, G.A. Sturrock, S.A. Penkett, C.A.M. Brenninkmeijer, V. Gros, J. Williams, H.A. Scheeren, Nature 421 (2003) 131–135.
[5] B. Li, L. Li, K. Lin, W. Zhang, S. Lu, Q. Luo, Ultrason. Sonochem. 20 (2013) 855–863.
[6] B. Li, K. Lin, W. Zhang, S. Lu, Y. Liu, J. Environ. Eng. 138 (2012) 903–914.
[7] T.- Tseng, H. Chu, H.- Hsu, Environ. Sci. Technol. 37 (2003) 171–176.
[8] J.W. Gander, G.F. Parkin, M.M. Scherer, Environ. Sci. Technol. 36 (2002) 4540–4546.
[9] D. Wu, Z. Yang, W. Wang, G. Tian, S. Xu, A. Sims, Chemosphere 88 (2012) 1108–1113.
[10] X. Wang, C. Chen, Y. Chang, H. Liu, J. Hazard. Mater. 161 (2009) 815–823.
[11] B. De Rivas, R. López-Fonseca, C. Jiménez-González, J.I. Gutiérrez-Ortiz, J. Catal. 281 (2011) 88–97.
[12] B. de Rivas, C. Sampedro, M. García-Real, R. López-Fonseca, J.I. Gutiérrez-Ortiz, Appl. Catal. B 129 (2013) 225–235.
[13] N. Blanch-Raga, M.D. Soriano, A.E. Palomares, P. Concepción, J. Martínez-Triguero, J.M.L. Nieto, Appl. Catal. B 130–131 (2013) 36–43.
[14] T. Cai, H. Huang, W. Deng, Q. Dai, W. Liu, X. Wang, Appl. Catal. B 166–167 (2015) 393–405.
[15] S.- Chen, Y. Wang, A.- Jia, H.- Liu, M.- Luo, J.- Lu, Appl. Surf. Sci. 307 (2014) 178–188.
[16] Q. Dai, S. Bai, Z. Wang, X. Wang, G. Lu, Appl. Catal. B 126 (2012) 64–75.
[17] Y. Wang, A.- Jia, M.- Luo, J.- Lu, Appl. Catal. B 165 (2015) 477–486.
[18] C. Zhang, C. Wang, W. Zhan, Y. Guo, Y. Guo, G. Lu, A. Baylet, A. Giroir-Fendler, Appl. Catal. B 129 (2013) 509–516.
[19] R. López-Fonseca, J.I. Gutiérrez-Ortiz, J.R. González-Velasco, Appl. Catal. A 271 (2004) 39–46.
[20] B.H. Aristizábal, C. Maya, C.M.D. Correa, Appl. Catal. A 335 (2008) 211–219.
[21] X.Y. Wang, Q. Kang, D. Li, Appl. Catal. B 86 (2009) 166–175.
[22] K. Poplawski, J. Lichtenberger, F.J. Keil, K. Schnitzlein, M.D. Amiridis, Catal. Today 62 (2000) 329–336.
[23] X.D. Ma, Q. Sun, X. Feng, X. He, J. Guo, H.W. Sun, H.Q. Cao, Appl. Catal. A 450 (2013) 143–151.
[24] M. Gallastegi-Villa, A. Aranzabal, Z. Boukha, J.A. González-Marcos, J.R. González-Velasco, M.V. Martínez-Huerta, M.A. Bañares, Catal. Today 254 (2015) 2–11.
[25] P.S. Chintawar, H.L. Greene, Appl. Catal. B 13 (1997) 81–92.
[26] W. Chu, P.A. Chernavskii, L. Gengembre, G.A. Pankina, P. Fongarland, A.Y. Khodakov, J. Catal. 252 (2007) 215–230.
[27] Z. Boukha, M. Kacimi, M.F.R. Pereira, J.L. Faria, J.L. Figueiredo, M. Ziyad, Appl. Catal. A 317 (2007) 299–309.
[28] Z. Boukha, M. Kacimi, M. Ziyad, A. Ensuque, F. Bozon-Verduraz, J. Mol. Catal. A 270 (2007) 205–213.
[29] J. Huang, L.- Wang, Y.- Liu, Y. Cao, H.- He, K.- Fan, Appl. Catal. B 101 (2011) 560–569.
[30] K. Elkabouss, M. Kacimi, M. Ziyad, S. Ammar, F. Bozon-Verduraz, J. Catal. 226 (2004) 16–24.
[31] Y. Feng, H. Yin, D. Gao, A. Wang, L. Shen, M. Meng, J. Catal. 316 (2014) 67–77.
[32] J. Huang, L.- Wang, Y.- Liu, Y. Cao, H.- He, K.- Fan, Appl. Catal. B 101 (2011) 560–569.
[33] A. Mitsionis, T. Vaimakis, C. Trapalis, N. Todorova, D. Bahnemann, R. Dillert, Appl. Catal. B 106 (2011) 398–404.
[34] S. Ogo, A. Onda, Y. Iwasa, K. Hara, A. Fukuoka, K. Yanagisawa, J. Catal. 296 (2012) 24–30.
[35] Y. Matsumura, J.B. Moffat, Catal. Lett. 39 (1996) 205–208.
[36] W.T. Reichle, J. Catal. 17 (1970) 297–305.
[37] B. Aellach, A. Ezzamarty, J. Leglise, C. Lamonier, J.-F. Lamonier, Catal. Lett. 135 (2010) 197–206.
[38] D.C. Carvalho, L.G. Pinheiro, A. Campos, E.R.C. Millet, F.F. de Sousa, J.M. Filho, G.D. Saraiva, E.C.d.S. Filho, M.G. Fonseca, A.C. Oliveira, Appl. Catal. A 471 (2014) 39–49.
[39] M. Sudhakar, V.V. Kumar, G. Naresh, M.L. Kantam, S.K. Bhargava, A. Venugopal, Appl. Catal. B 180 (2016) 113–120.
[40] S. Sugiyama, H. Matsumoto, H. Hayashi, J.B. Moffat, Appl. Catal. B 20 (1999) 57–66.
[41] C. Wen, Y. Cui, X. Chen, B. Zong, W.- Dai, Appl. Catal. B 162 (2015) 483–493.
[42] E. Landi, A. Tampieri, G. Celotti, S. Sprio, J. Eur. Ceram. Soc. 20 (2000) 2377–2387.
[43] A. Solhy, W. Amer, M. Karkouri, R. Tahir, A. El Bouari, A. Fihri, M. Bousmina, M. Zahouily, J. Mol. Catal. A 336 (2011) 8–15.
[44] M. Tamai, K. Isama, R. Nakaoka, T. Tsuchiya, J. Artif. Organs. 10 (2007) 22–28.
[45] A. Griboval-Constant, A. Butel, V.V. Ordomsky, P.A. Chernavskii, A.Y. Khodakov, Appl. Catal. A 481 (2014) 116–126.
[46] H.- Kim, L.- Li, Y.- Koh, J.C. Knowles, H.- Kim, J. Am. Ceram. Soc. 87 (2004) 1939–1944.
[47] J.- Han, H.- Song, F. Saito, B.- Lee, Mater. Chem. Phys. 99 (2006) 235–239.
[48] F. Kurtulus, H. Güler, Inorg. Mater. 41 (2005) 483–485.
[49] D. Li, D. Yang, X. Zhu, D. Jing, Y. Xia, Q. Ji, R. Cai, H. Li, Y. Che, J. Mater. Chem. A 2 (2014) 18761–18766.
[50] M.- Chen, W. Chu, J.- Zhu, L. Dong, J. Sol Gel Sci. Technol. 47 (2008) 354–359.
[51] J. Jiu, Y. Ge, X. Li, L. Nie, Mater. Lett. 54 (2002) 260–263.
[52] P. Jones, J.A. Hockey, Trans. Faraday Soc. 67 (1971) 2679.
[53] A.A. Verberckmoes, B.M. Weckhuysen, R.A. Schoonheydt, Micropor. Mesopor. Mater. 22 (1998) 165–178.
[54] Y. Brik, M. Kacimi, M. Ziyad, F. Bozon-Verduraz, J. Catal. 202 (2001) 118–128.
[55] F. Bozon-Verduraz, F. Fiévet, J.- Piquemal, R. Brayner, K.E. Kabouss, Y. Soumare, G. Viau, G. Shafeev, Braz. J. Phys. 39 (2009) 134–140.
[56] Z. Boukha, C. Jiménez-González, B. de Rivas, J.R. González-Velasco, J.I. Gutiérrez-Ortiz, R. López-Fonseca, Appl. Catal. B 158–159 (2014) 190–201.
[57] B. de Rivas, R. Lopez-Fonseca, J.R. Gonzalez-Velasco, J.I. Gutierrez-Ortiz, J. Mol. Catal. Catal. A 278 (2007) 181–188.
[58] J. Zhou, L. Zhao, Q. Huang, R. Zhou, X. Li, Catal. Lett. 127 (2009) 277–284.
[59] B. de Rivas, R. López-Fonseca, C. Jiménez-González, J.I. Gutiérrez-Ortiz, Chem. Eng. J. 184 (2012) 184–192.